

Article

Improving the Inertial Response of a Grid-Forming Voltage Source Converter

Juan Dolado ^{1,*}, Jose Luis Rodríguez Amenedo ^{1,*}, Santiago Arnaltes ^{1,*} and Joaquín Eloy-García ^{2,*}

¹ Electrical Engineering Department, Superior Polytechnique School, Faculty of Engineering, Carlos III University of Madrid, 28911 Madrid, Spain

² Ingenia Power Solutions SL, 28108 Madrid, Spain

* Correspondence: jdolado@ing.uc3m.es (J.D.); amenedo@ing.uc3m.es (J.L.R.A.); arnalte@ing.uc3m.es (S.A.); jeloygar@ing.uc3m.es (J.E.-G.)

Abstract: In recent years, the use of synchronous generators (SGs) has been displaced due to the increased use of renewable energy sources. These types of plants mostly use power electronic converters to connect to power grids, which, due to their mode of operation, cannot provide the same services. This paper analyzes the synchronization of Grid-Forming converters (GFM) without phase-locked loop (PLL) through the active power control loop. Stability analysis shows that when increasing the emulated moment of inertia in a voltage source converter (VSC) using grid-forming control, the system becomes oscillatory. The paper proposes a novel compensation mechanism in order to damp the system oscillation, allowing the implementation of inertia emulation. Finally, the real-time implementation is executed using a Hardware in the Loop experimental set-up. The response of VSC under grid disturbances is simulated in a real time simulator, while the proposed control system is implemented in a real-time controller platform.

Keywords: grid-forming power converter; power synchronization; renewable energy sources; inertia emulation; hardware in the loop



Citation: Dolado, J.; Rodríguez

Amenedo, J.L.; Arnaltes, S.;

Eloy-García, J. Improving the Inertial Response of a Grid-Forming Voltage Source Converter. *Electronics* **2022**, *11*, 2303. <https://doi.org/10.3390/electronics11152303>

Academic Editor: Khaled Ahmed

Received: 27 June 2022

Accepted: 21 July 2022

Published: 23 July 2022

Publisher's Note: MDPI stays neutral with regard to jurisdictional claims in published maps and institutional affiliations.



Copyright: © 2022 by the authors. Licensee MDPI, Basel, Switzerland. This article is an open access article distributed under the terms and conditions of the Creative Commons Attribution (CC BY) license (<https://creativecommons.org/licenses/by/4.0/>).

1. Introduction

Nowadays, it is a well-known fact that the high penetration of renewable power plants has completely changed the electrical generation model. Only 25 years ago, the vast majority of power plants were based on thermal, hydraulic and nuclear energy sources that used a conventional SG as electromechanical power converters to grid connection. Unlike this concept, renewable energy (wind farms and photovoltaic power plants) has arisen as an alternative to traditional power stations, but with some important particularities. On the one hand, renewable energy sources (RES) interact with the grid through inverter-based resources (IBRs) that differ from conventional SGs in that they do not behave as voltage sources but as constant power sources [1].

According to the latest studies [2], RES hourly penetration scenarios close to 100% are already taking place in some power systems. It seems clear that in a system in which most or all resources are inverter-based, these must contribute to grid services to ensure system stability and reliability. The displacement of SGs by IBRs can result in degrading power system stability and operability if IBRs do not provide the same services as SGs. Ancillary services required to operate a stable and secure grid can be grouped into different categories, such as: inertial response, frequency control, voltage control, system strength and power system restoration, among others [3].

Unlike SGs, inverter-based RES currently require a stable voltage at their terminals to exchange active power with the network converting the variable energy resource into electrical energy. Likewise, they also have the capacity to exchange reactive power, contributing to power factor control and voltage regulation. This requirement of having a stable voltage at their terminals is guaranteed mainly by the voltage and frequency regulation provided by

SGs. For that reason, these types of converters are usually named as grid-following (GFL) converters. Its operating principle is based on the estimation of the magnitude and phase of the voltage at their terminals by means of a Phase-Locked Loop (PLL). Although this voltage measurement and estimation technique has been improved over the years, allowing the proper operation of GFL converters in grids with a high content of voltage harmonics or imbalances, GFL converters are not adequate for operation on weak grids with low short-circuit power. Furthermore, GFL converters have a reduced ability to provide inertial response and they are not able to operate in islanded mode, so they cannot contribute to the restoration of the power system in the event of a blackout [4]. GFL converters cannot provide certain services required for the electrical system operation, therefore a new type of technology, grid-forming GFM converters, have been recently developed. Its principle of operation is based on reproducing the same behavior as a SG, keeping the module and phase of its internal voltage controlled, even during sub-transient periods. GFM converters are able to operate in isolated mode and in networks with very low short-circuit power, contributing to the power system restoration service. Furthermore, they are able not only capable of damping power oscillations but also of providing inertial response [5].

Different grid-forming converter implementations can be found in the bibliography. According to its operation principles, they can be grouped into three categories [6]. First category corresponds to the droop control concept which enables the parallel operation of multiple converters emulating the governor action of SGs. This category can be subdivided into a frequency-based droop [7–12], angle-based droop [13–15] or power synchronization control (PSC) [16,17]. One of the serious shortcomings of the droop controller is the lack of inertia support. Recently, new GFM controllers that incorporate the inertial and damping properties of SGs have been proposed, which have been included in the second category named synchronous-machine-based control. The first attempt at emulating the behavior of a SG was introduced as a concept called virtual synchronous machine (VISMA) [18,19], reproducing by control the complete dynamic equations of a SG. Some GFM controllers emulate the SG's swing equation [20–30], others operate as virtual synchronous generators (VSG) with augmented capabilities [31–38] in order to achieve better damping and improved transient stability. Another concept in this category is the Synchronverter that completely mimics the dynamics of a SG through control, including the electrical machine, speed governor and voltage regulator [39–44]. In [45–47], a novel GFM control strategy named matching control is presented. This new controller is designed to match the electromechanical energy transfer of SGs by utilizing the DC-link voltage of the converter. Apart from these two categories, some other non-linear methods are also proposed such as the virtual oscillation-based method [48–56]. The virtual oscillator controller (VOC) is a non-linear control strategy which makes a converter reproduce the dynamic of a weakly nonlinear limit-cycle oscillator, allowing converters to synchronize with each other from any arbitrary initial condition without the need for any communication.

Due to the inherent behavior of a GFM converter as a voltage source, this technology may encounter overcurrent problems under large grid disturbances such AC faults, phase jumps or large frequency deviations. For these cases, there are different current limiting strategies which are based on adding a current limiter block between voltage and current control [57–59], or more sophisticated ones based on virtual impedance control [60] and acting over the internal frequency on the power synchronization loop, avoiding the possibility of the GFM inverter becoming unstable.

This paper is focused on providing inertial response by a GFM converter using an internal power stabilizer in order to damp any power oscillation produced by the converter during grid frequency changes. These power oscillations are more pronounced when a high constant inertia and low damping factor are used without any stabilizer. GFM converters are considered a promising solution to address the challenges associated with the provision of emulated inertial response to support the operation of converter-dominated power systems. This inertia support can also be provided through a synchronous condenser (SC); however, this option presents some drawbacks in comparison to the GFM converter,

operating as a static synchronous condenser [61]. Conventional SCs based on a rotating synchronous machine is a well-known and mature technology, but its moment of inertia is constant and cannot be changed once it has been installed. On the contrary, a static SC based on the GFM converter can modify its inertial response by control and modifying the required DC energy. In any case, this option is much more flexible than a conventional SC.

This paper is organized as follows. In Section 2 the system description including a VSC along with their voltage and current regulators is presented. Section 3 shows the GFM control strategy based on a power synchronization loop with a power stabilizer in order to design a static synchronous condenser providing inertial response. In Section 4, a current limiting strategy of the grid-forming converter is presented. Finally, in Section 5, the results of a comprehensive real time simulation are shown and discussed. The complete GFM control is executed using a hardware in the loop experimental set-up connected to a real-time digital simulator, where the response of the VSC operating as a static SC is analyzed under different grid disturbances. In Section 5, the final conclusions of this work are presented.

2. System Description and Control

This section describes the elements of a grid-connected voltage source converter, its dynamic equations and its control when operating as a grid-forming converter. Figure 1 illustrates a single line diagram of a VSC connected to the point of common coupling (PCC) through an LCL filter which includes a step-up transformer. The voltage at the DC bus terminals is V_{dc} , and the input current is I_{dc} .

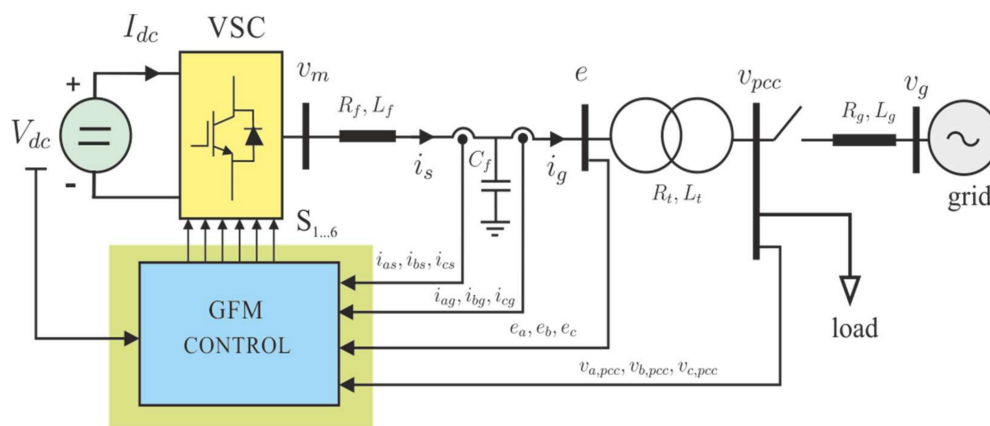


Figure 1. System description of a GFM-controlled VSC connected to a grid.

The VSC is controlled by measuring the three-phase current output of the converter, i_{as}, i_{bs}, i_{cs} , and the grid currents, i_{ag}, i_{bg}, i_{cg} . At the AC side, voltages in the capacitor C_f , e_a, e_b, e_c , and at the PCC $v_{a,pcc}, v_{b,pcc}, v_{c,pcc}$, are also required. At the DC side, the voltage V_{dc} is also measured. All these signals are the inputs of a GFM control block that determines the switching pattern $S_{1..6}$ from which the output voltages of the VSC v_{am}, v_{bm}, v_{cm} are generated. A breaker is connected between the PCC and the grid, and its state determines the operation mode of the VSC (on: grid connected, off: islanded). At the PCC, a local load is connected. The grid is modeled through a Thévenin equivalent formed by a three-phase voltage source v_{ag}, v_{bg}, v_{cg} of constant frequency ω_0 (rad/s), and an internal impedance with resistance R_f and reactance $\omega_0 L_f$.

2.1. Dynamic Equations

The dynamic equations of the VSC correspond to its LCL filter. These equations are represented in a rotating dq-axes system whose angular position, with respect to a stationary

reference system, θ , is determined by the GFM control. Using a vector representation in the dq-axes, the following dynamic equations of currents in the inductive filter, L_f , are obtained

$$v_{dm} - e_d = L_f \frac{di_{ds}}{dt} + R_f i_{ds} - \omega_0 L_f i_{qs}, \tag{1}$$

$$v_{qm} - e_q = L_f \frac{di_{qs}}{dt} + R_f i_{qs} + \omega_0 L_f i_{ds}. \tag{2}$$

Following the same procedure as above, the dynamic equations of dq voltages on the capacitor C_f are

$$i_{ds} - i_{dg} = C_f \frac{de_d}{dt} - \omega_0 C_f e_q, \tag{3}$$

$$i_{qs} - i_{qg} = C_f \frac{de_q}{dt} + \omega_0 C_f e_d. \tag{4}$$

As in (1) and (2), a similar representation for the variable states i_{dg} and i_{qg} can be obtained. In this case, the dynamic equations are as follows

$$e_d - v_{d,pcc} = L_t \frac{di_{dg}}{dt} + R_t i_{dg} - \omega_0 L_t i_{qg}, \tag{5}$$

$$e_q - v_{q,pcc} = L_t \frac{di_{qg}}{dt} + R_t i_{qg} + \omega_0 L_t i_{dg}. \tag{6}$$

2.2. Voltage and Current Controllers

A GFM-controlled VSC acts as a voltage source defined by its module, e , and its angle θ . Figure 2 shows the voltage and current control blocks to achieve the voltage source defined by e and θ up to obtaining the switching pattern $S_{1...6}$ of the VSC. Since the control is performed in the dq-axes, all instantaneous voltage and current variables are initially passed through a Park transformation $P(\theta)$ to obtain their dq components. Note that the angle θ used for the Park transformation corresponds to the angle reference of the voltage source. Its value will be determined through an active power synchronization loop, as explained in the following sections. Certainly, this is a differentiating aspect between GFM control and grid-following methods that use a PLL to determine this angle θ .

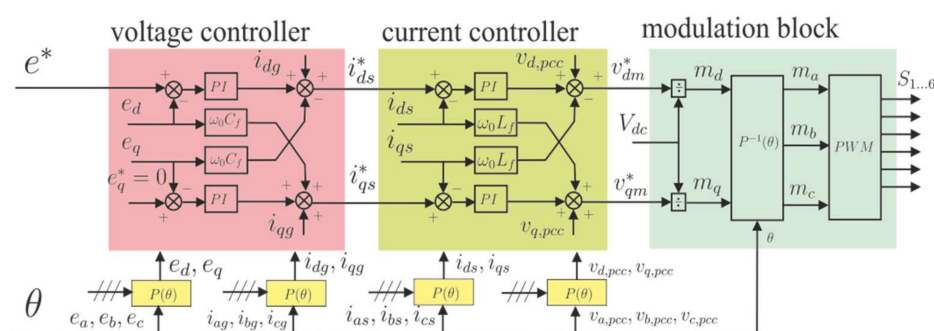


Figure 2. Grid-forming voltage and current control blocks.

In the outer voltage controller, the d-axis voltage reference, e^* , is compared to e_d , and likewise the q-axis reference, which is equal to zero, is compared to e_q . This means that the GFM control tries to align the voltage vector \vec{e} to the d-axis of the rotating dq reference system. The difference in these signals on each axis are inputs of two PI regulators that determine currents i_{ds}^* and i_{qs}^* , respectively. According to (3) and (4), these dq currents components are compensated by two cross-coupling terms, $-\omega_0 C_f e_q$ and $\omega_0 C_f e_d$, which correspond to current dq-components on the capacitor, and by two additional current

terms i_{dg} and i_{qg} . When these compensation terms are applied, dynamics of PI regulators improve significantly.

A similar structure was used for the inner current controller. In this case, inputs are i_{ds}^* and i_{qs}^* , which are compared to the actual components i_{ds} and i_{qs} . These differences establish the voltage components v_{dm}^* and v_{qm}^* as the outputs of two PI regulators. As in the voltage controller, these components are obtained by adding two compensations terms. For the d-axis, this term is $v_{d,pcc} - \omega_0 L_f i_{qs}$, and for the q-axis $v_{q,pcc} + \omega_0 L_f i_{ds}$. Later on, these voltage components v_{dm}^* and v_{qm}^* are divided by V_{dc} (both magnitudes in p.u.) in order to obtain m_d and m_q , which are the d and q amplitude modulation indexes, respectively. By applying an inverse Park transformation, $P^{-1}(\theta)$, the amplitude modulation indices per phase m_a, m_b, m_c are obtained. Finally, through a pulse width modulation (PWM) of these three-phase magnitudes the switching pattern $S_{1\dots6}$ is achieved.

2.3. Reactive Power Controller

As shown in Figure 2, the internal voltage reference is defined by its module, e^* , and its angle θ . These references are usually calculated through external power controllers, so that the VSC can be operated as a PQ node, or eventually as a PV node if the reactive power controller is replaced by a voltage controller.

Figure 3 shows a reactive power controller. The controller is based on the well-known droop control where the voltage magnitude e^* is obtained as the product of a gain constant, n_q , times the difference between the reactive power reference, Q^* , and its actual value, Q , plus an initial voltage e_0

$$e^* = e_0 - n_q(Q - Q^*). \tag{7}$$

This equation can be interpreted as follows. When the reactive power is greater than its reference, $Q > Q^*$, it means that the voltage reference e^* is reduced below the voltage value e_0 so that the reactive Q decreases, achieving a steady-state value close to the reactive power reference Q^* . Since this is a proportional controller, this system can reach a stable operating point where Q and Q^* are different. Although this gives rise to an error in steady state, the advantage of this method is that several VSC converters can contribute to the voltage control by sharing reactive power proportionally to their rated power.

Figure 3 shows how the voltage reference e^* is affected by a signal Δe . This signal is different from zero only when the reactive current, I_{react} , is out of limits. One way of limiting the reactive current is achieved by acting over the voltage reference; decreasing e^* when I_{react} is greater than its maximum limit ($I_{react} > I_{react}^{max}$), or increasing e^* when it is lower than a minimum value (usually $I_{react}^{min} = -I_{react}^{max}$). In this figure, RCL represents the reactive current limiting block, shown in Figure 4.

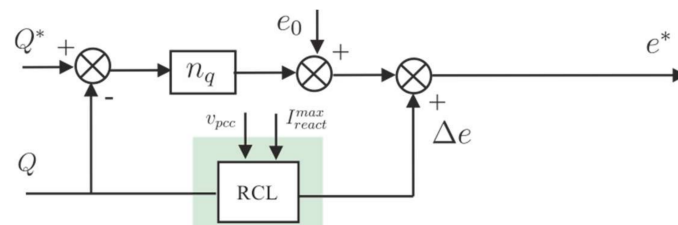


Figure 3. Reactive power controller.

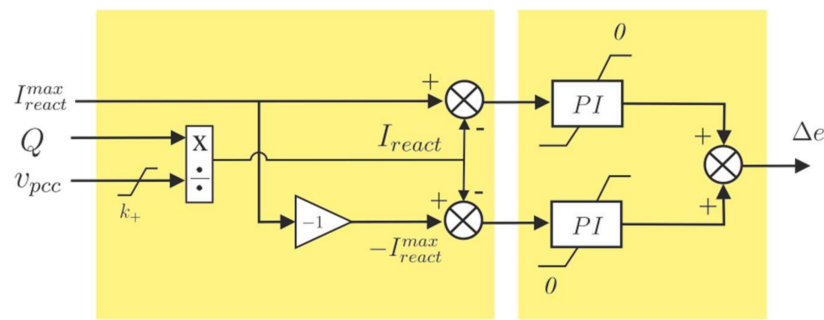


Figure 4. Reactive current limiting (RCL) block.

The reactive power injected by the VSC can be expressed as the product of voltage and current dq components as

$$Q = v_{q,pcc}i_{dg} - v_{d,pcc}i_{qg}, \tag{8}$$

where Q has been expressed in p.u. The reactive power can also be represented in terms of the product of the reactive current I_{react} and the voltage module at the PCC as

$$Q = v_{pcc}I_{react}. \tag{9}$$

Figure 4 shows the reactive current limiting block mentioned before. According to (9), the reactive current, I_{react} , is obtained by dividing Q by the module of the voltage at PCC v_{pcc} . To avoid numerical issues when $v_{pcc} = 0$, v_{pcc} is limited to a value greater than k_+ . In case the reactive current starts to be out of limits, e.g., when $I_{react} > I_{react}^{max}$ the PI regulator generates a negative Δe , decreasing the voltage reference e^* and therefore reducing I_{react} . On the other hand, when $I_{react} < -I_{react}^{max}$ regulator’s output establishes that $\Delta e = 0$.

A similar reasoning can be made for the lower limit $-I_{react}^{max}$. In this case, when the reactive current is out of limits, ($I_{react} < -I_{react}^{max}$) the PI regulator generates a positive $\Delta e > 0$, and, as before, $\Delta e = 0$ if ($I_{react} > -I_{react}^{max}$). A clear advantage of this type of limiter is that it only operates when the reactive current is out of limits. Otherwise, the voltage reference e^* is calculated by a reactive power controller, or by a PCC voltage regulator in case of operating in isolated mode.

2.4. Active Power Synchronization Loop

The active power synchronization loop is shown in Figure 5. The block diagram corresponding to the swing equation of the synchronous generator is expressed as a differential equation as follows

$$P^* - P = J \frac{d\omega'}{dt} + D(\omega' - \omega_0). \tag{10}$$

By integrating (10) the internal frequency ω' is obtained, where P^* and P are the reference and the measured active power of the VSC converter at PCC, respectively. The nominal frequency is represented by ω_0 , being J the moment of inertia, twice the inertial constant $J = 2H$, expressed in seconds, and D the damping factor which, in p.u., is inverse to the droop constant R , so that $D = 1/R$.

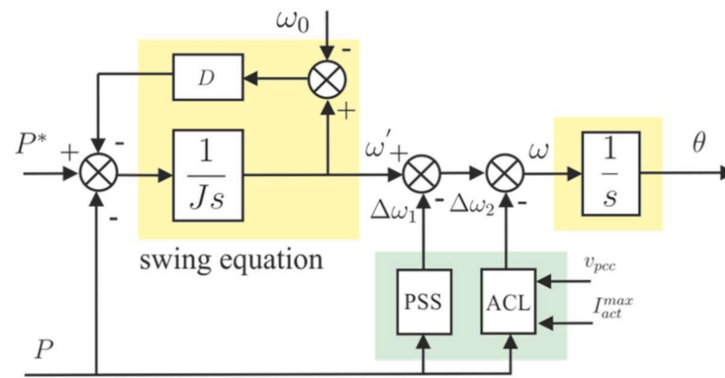


Figure 5. Active power synchronization loop.

The internal frequency ω' is integrated to obtain the control angle of the rotating dq axes. In fact, this internal frequency is corrected by signals $\Delta\omega_1$ and $\Delta\omega_2$, which are the outputs of a power system stabilizer (PSS), and an active current limiting block (ACL), respectively. So, the control angle is obtained as

$$\theta = \int \omega dt = \int [\omega' - (\Delta\omega_1 + \Delta\omega_2)] dt. \tag{11}$$

As before, the active power generated by the VSC in this case is expressed, in p.u., as the product of voltages and currents dq components as

$$P = v_{d,pcc}i_{dg} + v_{q,pcc}i_{qg} \tag{12}$$

and as the product of the voltage magnitude v_{pcc} and the active current I_{act}

$$P = v_{pcc}I_{act}. \tag{13}$$

Like in the previous case, the active current limiting block modify the control angle θ to avoid system instability if $\theta - \omega_0 t$ reaches a value greater than $\pi/2$ or lower than $-\pi/2$. Figure 6 shows this ACL block.

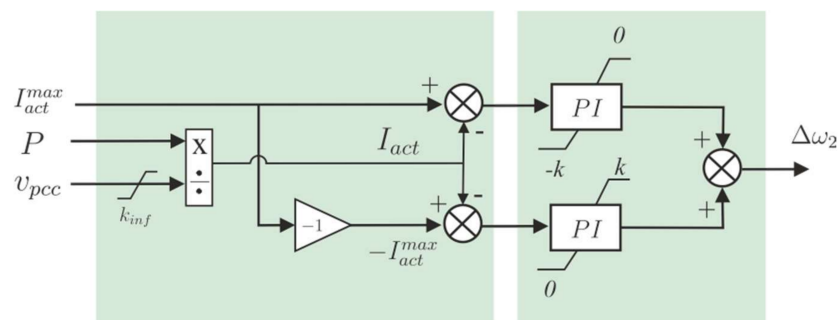


Figure 6. Active current limiting (ACL) block.

Its structure and control logic are similar to the RCL block but in this case using the active current I_{act} obtained from P . Furthermore, PI limits are saturated to a value $\Delta\omega_2 = -k$ when $I_{act} > I_{act}^{max}$ and $\Delta\omega_2 = +k$ when $I_{act} < -I_{act}^{max}$.

The next section presents the design and parameter tuning of the PSS shown in Figure 5.

3. Power System Stabilizer

This section discusses the design and tuning of a power system stabilizer (PSS) integrated in the active power synchronization loop as it shown in Figure 5, analyzing the

dynamic response of the control angle, $\Delta\delta$, with respect to changes in the active power reference $\Delta\bar{P}^*$ or on the grid frequency, $\Delta\bar{\omega}_g$. These are increment variables, or small signals around an equilibrium point. In particular, $\Delta\delta$ is the angular position deviation of the dq axes with respect to a reference frame rotating at ω_0 rad/s. Likewise, $\Delta\bar{P}^*$ is a deviation from the power reference \bar{P}^* on the equilibrium point, and $\Delta\bar{\omega}_g$ a frequency deviation from the grid frequency ω_g . Overline notation on these variables means that they are expressed in p.u.

The dynamic relationship between $\Delta\delta$ under changes on $\Delta\bar{P}^*$ and $\Delta\bar{\omega}_g$ is achieved by following a three-step process. Firstly, linearizing (10) around an operating point yields

$$\Delta\bar{P}^* - \Delta\bar{P} = (Js + D)\Delta\bar{\omega}', \tag{14}$$

from which a first-order transfer function $G(s)$ can be defined as

$$G(s) = \frac{\Delta\bar{\omega}'}{\Delta\bar{P}^* - \Delta\bar{P}} = \frac{1}{Js + D} \tag{15}$$

where J represents the moment of inertia of the virtual synchronous generator (VSG) in seconds and D the damping constant in p.u. The reciprocal of D is the droop constant

$$R = \frac{1}{D} = \frac{\Delta f / f_n}{\Delta P / P_n}, \tag{16}$$

which represents, in p.u., the coefficient between the variation in the frequency with respect to the nominal frequency and the variation in power with respect to the nominal power.

The second step is to calculate the angular increment $\Delta\delta$ as a function of $\Delta\bar{\omega}'$ and $\Delta\bar{\omega}_g$ as follows

$$\frac{1}{\omega_0} \frac{d\Delta\delta}{dt} = \Delta\bar{\omega}' - \Delta\bar{\omega}_g. \tag{17}$$

Its dynamic response depends on the difference between the internal frequency and the grid frequency. When the VSC is synchronized, the power-angle, δ , is constant and both frequencies, ω' and ω_g , are equal.

Figure 7 shows the block diagram of the active power synchronization loop where the dependency of $\Delta\bar{P}^*$ with $\Delta\delta$ through the function $P(\delta)$ is shown.

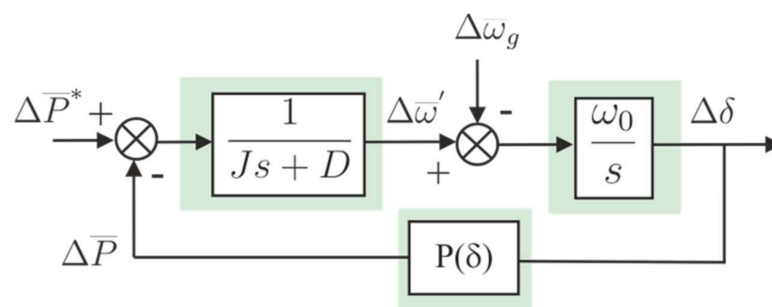


Figure 7. Block diagram of the active power synchronization loop.

It is a well-known fact that the active power transmitted between two nodes connected through a line is inversely proportional to the line reactance, and directly proportional to the voltage magnitude of the nodes and to $\sin\delta$, being δ the angular difference between these two nodes. Applying this definition to the active power transferred by the VSC of Figure 1 yields an expression for the active power as

$$\bar{P} = \left(\frac{v_m e}{X_f} \right) \sin\delta, \tag{18}$$

where X_f is the reactance of the output filter. By considering the increments in this equation, the following linear relationship between power and angle is obtained

$$\Delta \bar{P} = K_s \Delta \delta, \quad (19)$$

where K_s is the synchronizing constant and its value is obtained by applying to (18) the partial derivative of \bar{P} with respect to δ at the point of equilibrium "0"

$$K_s = \left(\frac{\partial \bar{P}}{\partial \delta} \right)_0 = \left(\frac{v_{m0} e_0}{X_f} \right) \cos \delta_0. \quad (20)$$

From the block diagram in Figure 7, the transfer function between $\Delta \delta$ and $\Delta \bar{P}^*$ (considering $\Delta \bar{\omega}_g = 0$) can be obtained as follows

$$\frac{\Delta \delta}{\Delta \bar{P}^*} = \frac{\omega_0}{Js^2 + Ds + K_s \omega_0}. \quad (21)$$

Similarly, the transfer function between $\Delta \delta$ and $\Delta \bar{\omega}_g$ when the power reference is constant $\Delta \bar{P}^* = 0$ can also be achieved. In this case, the power increment $\Delta \bar{P}$ is equal to

$$\Delta \bar{P} = \frac{\omega_0 K_s}{s} (\Delta \bar{\omega}' - \Delta \bar{\omega}_g). \quad (22)$$

considering that the internal frequency increment can be expressed in terms of $\Delta \bar{P}$ as

$$\Delta \bar{\omega}' = -\frac{\Delta \bar{P}}{Js + D}. \quad (23)$$

Substituting (23) in (22) yields

$$\frac{\Delta \bar{P}}{\Delta \bar{\omega}_g} = -\frac{\omega_0 K_s (Js + D)}{s(Js + D) + \omega_0 K_s} \quad (24)$$

and reordering, it can be expressed as the sum of two terms

$$\Delta \bar{P} = -\frac{\omega_0 K_s Js}{Js^2 + Ds + \omega_0 K_s} \Delta \bar{\omega}_g - \frac{\omega_0 K_s D}{Js^2 + Ds + \omega_0 K_s} \Delta \bar{\omega}_g \quad (25)$$

The first one corresponds to the inertial response, where the product $s \Delta \bar{\omega}_g$ is defined as the rate of change in frequency (RoCoF), so that the power injected in steady-state due to the inertial response is equal to

$$\Delta \bar{P}_{inertial} = -J \cdot (s \Delta \bar{\omega}_g) = -J \cdot \text{RoCoF}. \quad (26)$$

In other words, the power exchanged by the VSC-GFM during an inertial response is proportional to the moment of inertia, J , and to the RoCoF. Note that the power response has an opposite sign to frequency variations.

Considering now the second term and operating in the same way, the power increment in steady-state due to the droop response is

$$\Delta \bar{P}_{droop} = -D \cdot \Delta \bar{\omega}_g. \quad (27)$$

Considering an application where the GFM-VSC presents only an inertial response ($D = 0$), the dynamics under a change in frequency have two complex-conjugated poles on

the imaginary axis, with a critically stable response and an oscillatory response, and the relationship between $\Delta\delta$ and $\Delta\bar{\omega}_g$ is equal to

$$\frac{\Delta\delta}{\Delta\bar{\omega}_g} = -\frac{\omega_0 J s}{J s^2 + \omega_0 K_s} \tag{28}$$

For this inertial response to be acceptable, a PSS must be included in the dynamics. Figure 8 shows the proposed PSS integrated in the active power synchronization loop.

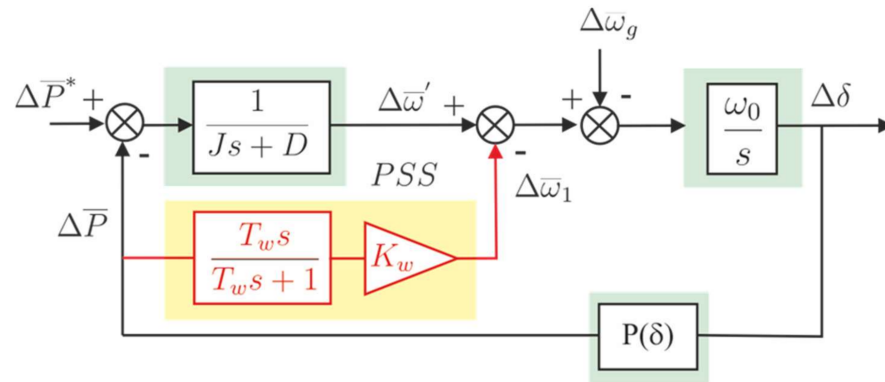


Figure 8. PSS integration in the power synchronization loop.

Representing (28) as a differential equation in terms of $\Delta\delta$ yields

$$J \frac{d^2(\Delta\delta)}{dt} + K_s \omega_0 \Delta\delta = -\omega_0 J \frac{d(\Delta\bar{\omega}_g)}{dt} \tag{29}$$

The PSS transfer function shown in Figure 8 can be expressed as

$$\frac{\Delta\bar{\omega}_1}{\Delta\bar{P}} = -K_w \left(\frac{T_w s}{T_w s + 1} \right) \tag{30}$$

and considering that according to (19), $\Delta\bar{P}$ is equal to $K_s \Delta\delta$ and the relationship between the angle and the frequency, (30) can be represented as follows

$$T_w \frac{d^2(\Delta\delta)}{dt} = -K_w K_s T_w \omega_0 \frac{d(\Delta\delta)}{dt}. \tag{31}$$

By adding (29) and (31), the following expression is obtained

$$[J + T_w] \frac{d^2(\Delta\delta)}{dt} + [K_w K_s T_w \omega_0] \frac{d(\Delta\delta)}{dt} + K_s \omega_0 \Delta\delta = -\omega_0 J \frac{d(\Delta\bar{\omega}_g)}{dt}, \tag{32}$$

that represents an equation similar to (28)

$$\frac{\Delta\delta}{\Delta\bar{\omega}_g} = -\frac{\omega_0 J s}{J' s^2 + D' s + \omega_0 K_s} \tag{33}$$

but with new values of inertia constant J' , and damping factor D' whose expressions are

$$J' = J + T_w \tag{34}$$

$$D' = K_w K_s (T_w \omega_0). \tag{35}$$

Note that J' depends on the PSS time constant T_w , but its influence is not relevant since J is usually higher than T_w . Typically, inertia constant values are in the order of seconds, while T_w is usually lower than 0.5 s. In the case of the damping constant D , its value is

mainly defined by the gain constant K_w . Once the plant is linearized, K_s is obtained, time constant T_w is defined and K_w is chosen to obtain a certain damping constant D' . When there is no PSS, $T_w = 0$ and equation (33) is the same as (28), being $J' = J$ and $D' = 0$.

Figure 9 shows the pole placement of the transfer function indicated in (33) as a function of K_w with the following parameters: the synchronizing constant K_s is equal to 6.67 p.u. considering a reactance X_f of 0.15 p.u. and at the operating point $v_{m0} = e_0 = 1$ p.u., and the power angle $\delta_0 = 0^\circ$; The PSS time constant is $T_w = 100$ ms and $\omega_0 = 100$ rad/s.

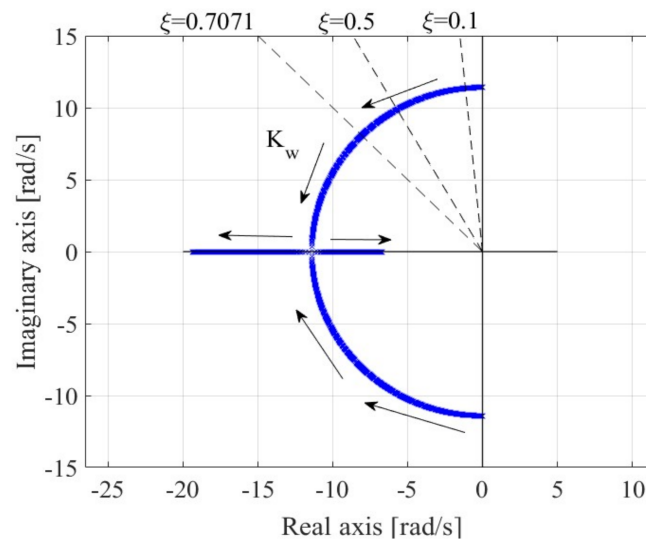


Figure 9. Poles loci of the transfer function $\Delta\delta/\Delta\bar{\omega}_g$ under K_w variation.

As shown in Figure 9, when $K_w = 0$ the damping factor is practically zero, the poles are complex conjugated and placed on the imaginary axis. When K_w increases, the poles follow a circular path in the negative half-plane until the damping ratio $\xi > 1$, from where the poles are placed on the negative real axis.

The natural frequency ω_n and the damping ratio ξ of a normalized second order function $s^2 + 2\xi\omega_n s + \omega_n^2$ of Equation (25) are calculated in terms of J , D , K_s and ω_0 as follows

$$\omega_n = \sqrt{\frac{\omega_0 K_s}{J}} \tag{36}$$

$$\xi = \frac{D}{2\sqrt{J\omega_0 K_s}} \tag{37}$$

The PSS parameters are adjusted by defining the time constant T_w and the PSS gain, K_w for a specific damping ratio ξ . Figure 10 shows K_w as a function of J , considering that $D = 0$ and $\xi = 0.7071$ (poles with equal real and imaginary part). K_s is equal to 6.67 p.u. and $\omega_0 = 100$ rad/s. As shown in the figure, when $J = 50$ s, $K_w = 0.51$ p.u. if $T_w = 0.4$ s and $K_w = 2.15$ p.u. for $T_w = 0.1$ s. So, in order to achieve the same damping ratio, the lower the time constant of the PSS, the higher its gain is.

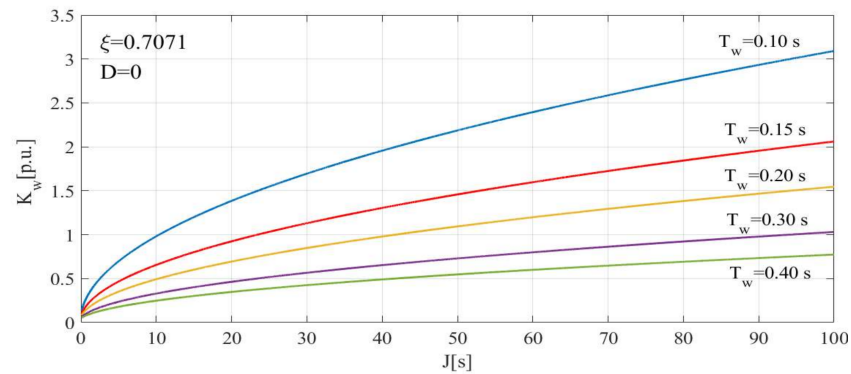


Figure 10. K_w as a function of J for different T_w values.

Figure 11 shows the response of GFM-VSC with and without PSS under a frequency drop of 2.5 Hz with a RoCoF of 0.3 Hz/s designed for an inertia constant $J = 60$ s and $D = 0$. This figure clearly shows the effect of the PSS, stabilizing the system response against a frequency variation.

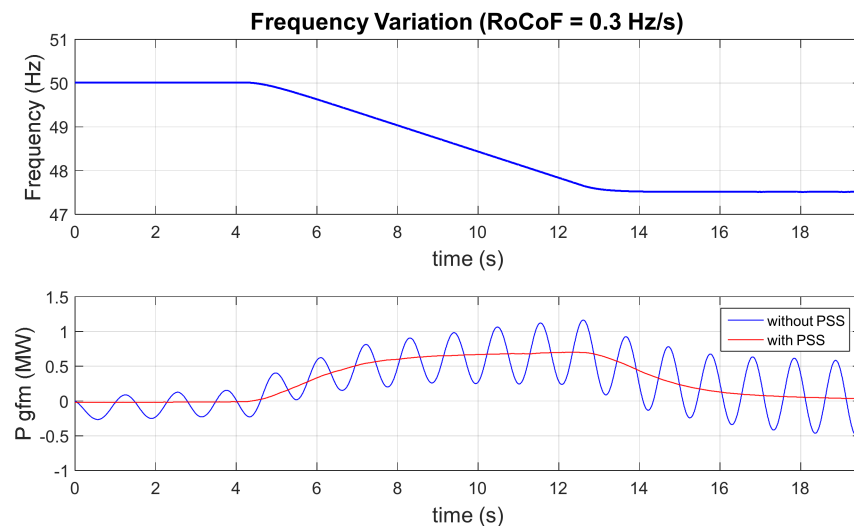


Figure 11. Active power provided by the VSC at a frequency variation with and without PSS.

Figure 12 shows the power provided by a 2 MW-VSC including a PSS under the same frequency variation for different values of the inertia constant J . To obtain these results, the converter was connected to an ideal network and a frequency drop of 2.5 Hz with a RoCoF of 0.3 Hz/s was applied. According to (26), the active power exchange by a GFM-VSC, designed to provide inertial response, is proportional to the inertia constant and to the rate of change in frequency. As shown in Figure 12, the active power increases when the frequency is reduced at a constant rate of 0.3 Hz/s. Only when the frequency is changing is the active power different from zero. In the interval where the frequency is changing, the higher the inertia, the higher the power generated.

The results shown in Figure 12 were obtained using the Hardware in the Loop experimental set-up, which will be described in the next section.

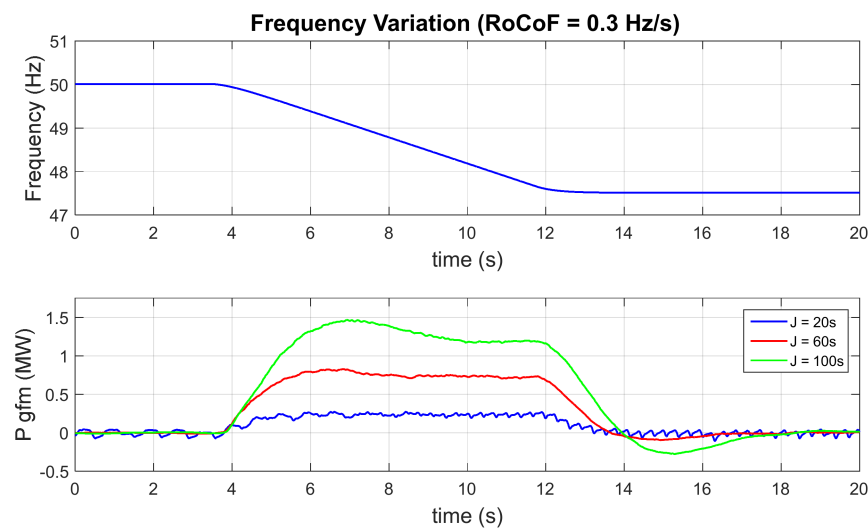


Figure 12. Active power provided by the VSC at a frequency variation for different J values.

4. Simulations Results

This section presents the performed tests, which include synchronization with the grid, response to load changes, operation in islanded mode and an analysis of the harmonic components of the converter voltage and current. In addition, the operation of the current limiter was also tested. For this purpose, the plant illustrated in Figure 13 has been modelled in RSCAD. This system consists of a SG that can be connected or disconnected to the PCC through a main switch (SW). The load can also be varied in order to check the converter behavior by means of another manually controlled switch, not represented in the scheme.

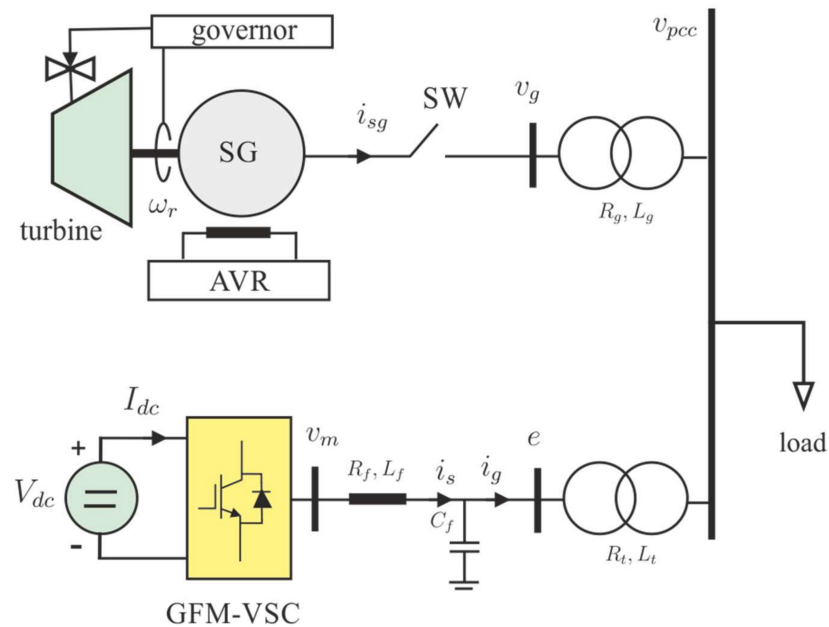


Figure 13. Schematic of the plant designed in RSCAD.

All the results presented in this section were obtained using the Hardware in the Loop experimental set-up shown in Figure 14, which includes the Real Time Digital Simulator (RTDS) on the left side of the image and the real-time controller (dSpace) on the right side.



Figure 14. Hardware in the Loop experimental set-up.

The parameters used to configure the model in RSCAD are given in Table A1 of Appendix A. Likewise, the parameters of the active power synchronization loop are given in Table A2 of Appendix B.

4.1. Synchronization

The state of the main switch is represented in the upper plot of Figure 15. The middle plot shows the phase a of the grid voltages and the converter voltages. Only one phase is represented to improve the presentation of the synchronization moment. Finally, the lower graph shows the error between these voltages ($Error = V_{a_{gfm}} - V_{a_{grid}}$). Before closing the main switch, the grid and the converter voltages are almost in phase and with a similar amplitude. At time $t = 0.06$ s, the main switch closes and the voltages of the GFM converter (in blue) and the grid (in red) are completely synchronized and the error becomes 0.

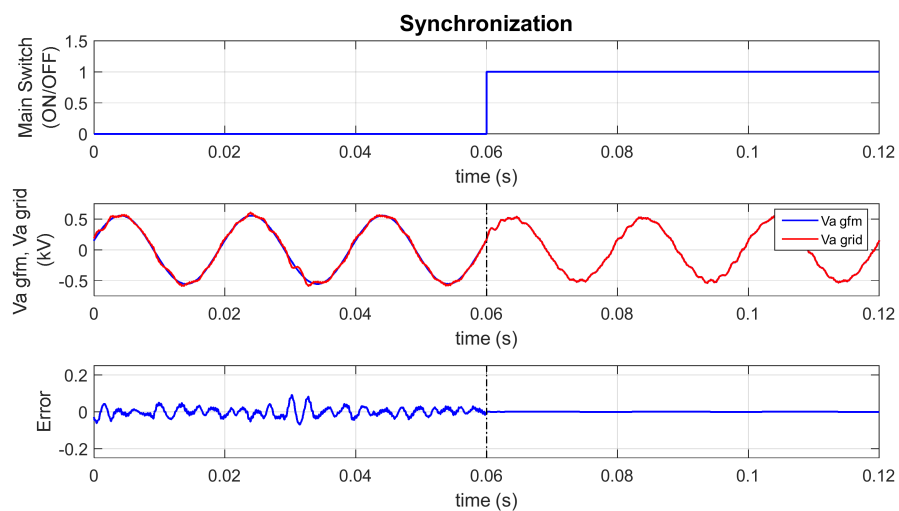


Figure 15. Grid synchronization signal and GFM converter voltages.

4.2. Load Change

Once the synchronization is verified, a load change is applied to check the response to a load disturbance. Figure 16 shows the load change, followed by the system frequency response and the active power supplied by the converter to support the system frequency.

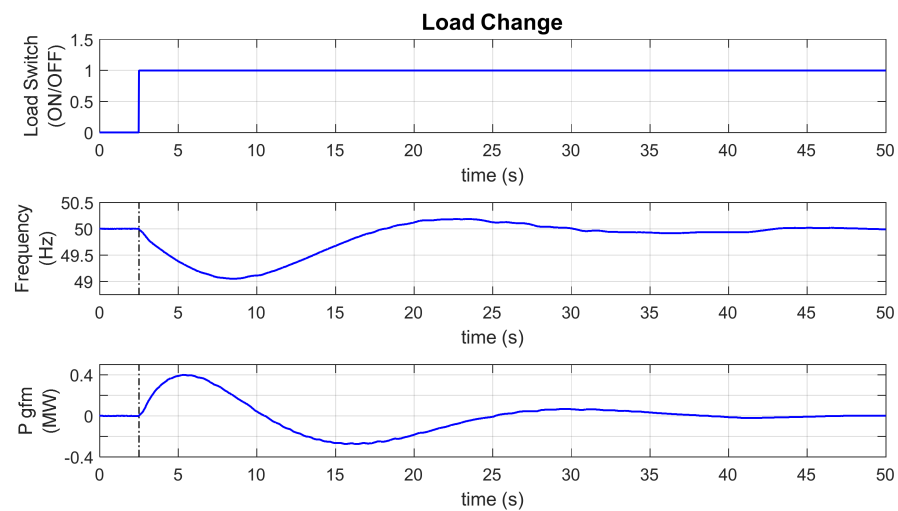


Figure 16. Power contribution by the converter at load change.

As soon as the load change occurs, the frequency decreases and, at the same time, the converter starts to inject active power to the grid. Likewise, when the grid begins to increase its frequency to reach 50 Hz again, the converter absorbs power to stabilize the system. Clearly, the converter power follows the frequency derivative to support the system frequency stability.

Figure 17 shows the comparison between the frequency response of the SG with and without a Grid-Forming converter support. The converter clearly helps to improve the RoCoF from 0.8 to 0.15 Hz/s, as well as the frequency nadir, which improved from 48.25 Hz to 49 Hz when the VSC was connected.

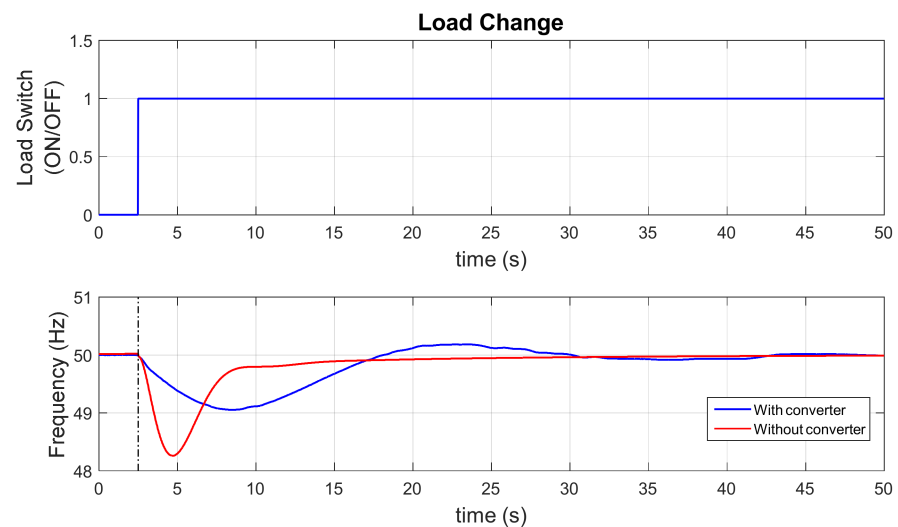


Figure 17. Comparison of frequency response with and without Grid-Forming converter.

4.3. Current Limiter

To test the operation of the current limiter, the converter was connected to an ideal source as in Section 3 and a frequency drop of 2.5 Hz with a RoCoF = 1 Hz/s was applied. In this case, a more abrupt frequency change was applied to reach the converter current limit. Figure 18 shows how during the frequency variation, the converter injects power to the grid which causes an increase in the current, saturating it to its maximum value, set at 1.15 times the value of the base current ($I_b = 2366.67 \text{ A}$, $I_{max} = 2721.67 \text{ A}$). The second graph shows the value of the current magnitude in p.u. and the last one, the instantaneous value of the three phase currents at the output of the converter, i_{as} , i_{bs} , i_{cs} .

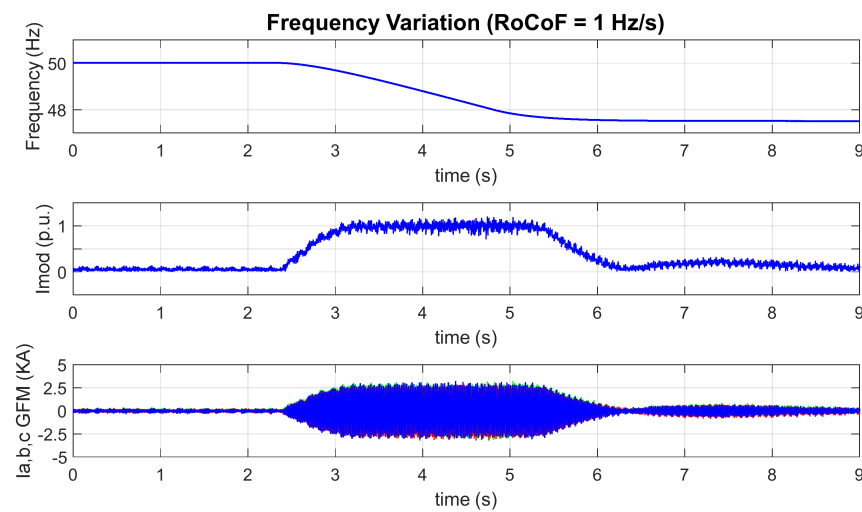


Figure 18. Verification of the operation of the current limiter.

4.4. Islanded Operation Mode

The capability to operate as a voltage source when the converter switches from grid-connected to islanded mode is an operational requirement for GFM converters. For this test, once the generator and the converter are synchronized and the load is connected, the SG is disconnected from the grid in $t = 0.5$ s to check the converter’s islanding mode operational capability. As shown in Figure 19, once the main switch is open, the converter can maintain the system voltage and frequency.

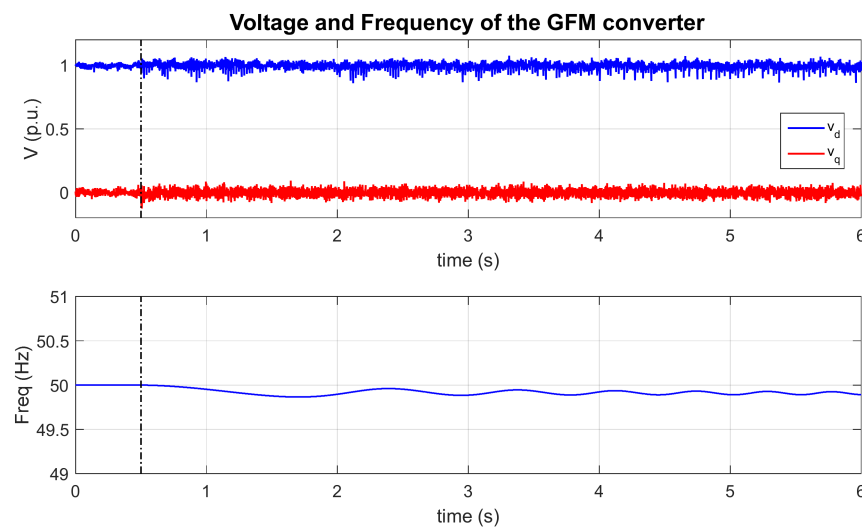


Figure 19. Voltage and frequency during the transition to islanded mode.

Figure 20 shows the instantaneous phase voltages before and after opening the main breaker. As in Figure 19, the voltages are almost unchanged when the converter switches to islanded mode.

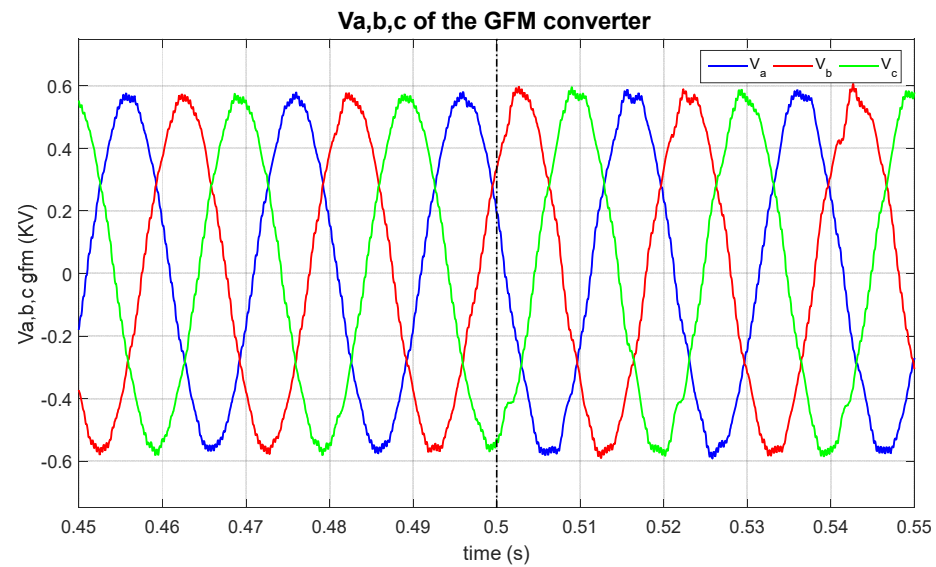


Figure 20. Instantaneous phase voltages during the transition to islanded mode.

When a GFM converter switches to islanded mode, it must, in addition to keeping the voltage and frequency under control, generate the active and reactive power demanded by the load. System load is 1 MW, as can be seen in Figure 21. Initially, the VSC power command is null, but when the switch is open the VSC automatically provides the system load, ($P_{gfm} = 1 \text{ MW}$), while the generator stops supplying it ($P_g = 0 \text{ MW}$).

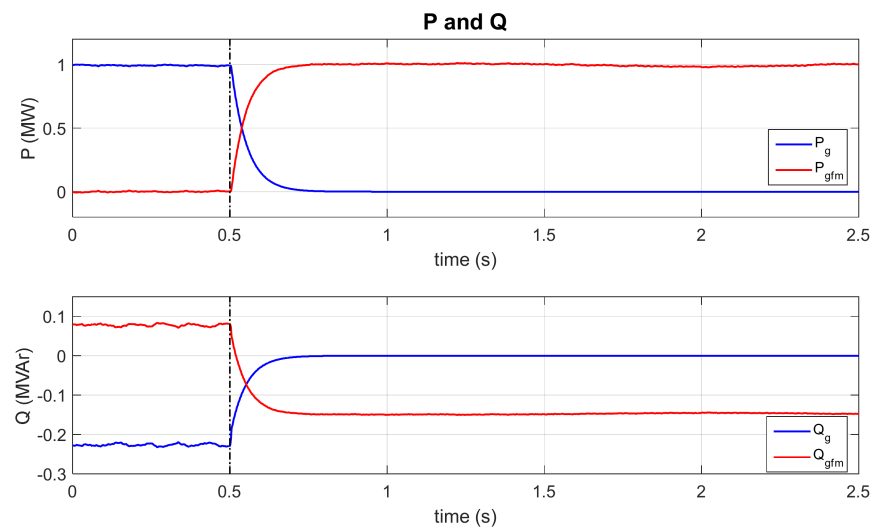


Figure 21. Active and reactive powers during the transition to islanded mode.

The reactive power response is given in the lower graph. Similarly, when the converter switches to islanded mode, the SG stops supplying the system reactive power ($Q_g = 0 \text{ MVar}$), which must be supplied by the VSC ($Q_{gfm} = -0.15 \text{ MVar}$ approx.). Note that in this case, the final reactive power is not the same, because when the switch is open, the SG step-up transformer is also disconnected, changing the system reactive power demand.

Finally, Figure 22 shows the instantaneous phase currents of the grid in the upper graph and those of the converter in the lower graph. It can be clearly seen that the grid currents become zero when the breaker is open, while the converter currents increase to supply the system demand.

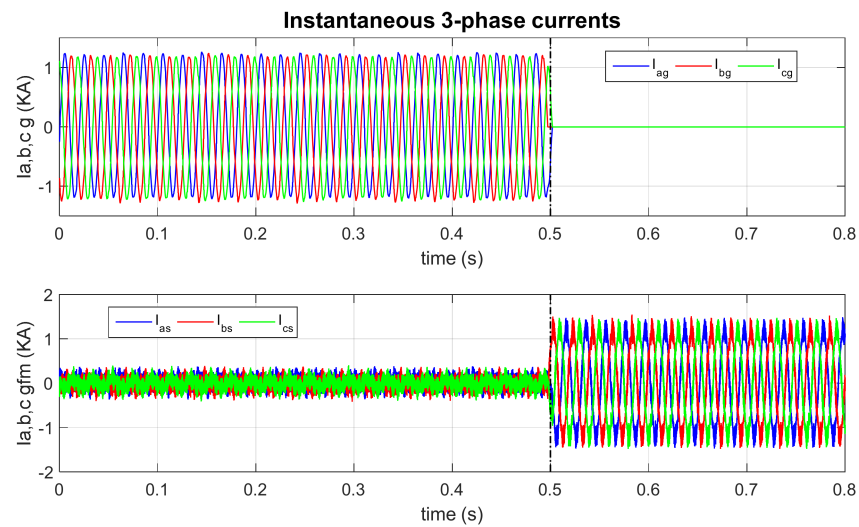


Figure 22. Instantaneous 3-phase currents during the transition to islanded mode.

4.5. Harmonic Analysis

For the analysis, the converter was first synchronized with the grid and then a 0.5 p.u. active power setpoint (1 MW) was sent. Figure 23 shows the converter generated voltage measured at the capacitor terminals and the current of phase a of the converter in the steady state.

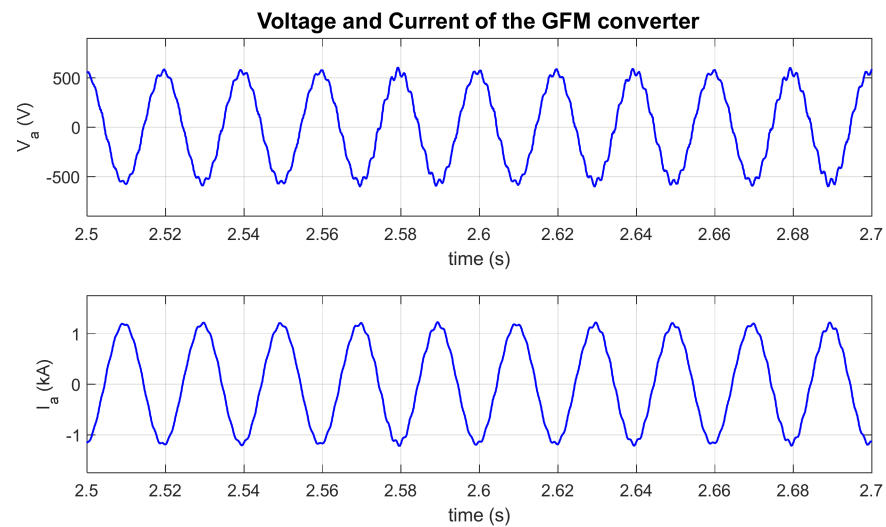


Figure 23. Inverter voltage and current of phase a of the converter in steady state.

The harmonic spectrum measurements presented in Figure 24 were performed according to Section 7.3 of IEEE 1547 and were normalized with respect to current I_n . The maximum harmonic current distortion limits in the percent of rated current for odd and even harmonics according to IEEE standards are represented in red and their values are given in Tables A3 and A4 of Appendix C. Lastly, the Total Harmonic Distortion value THD_i was also included.

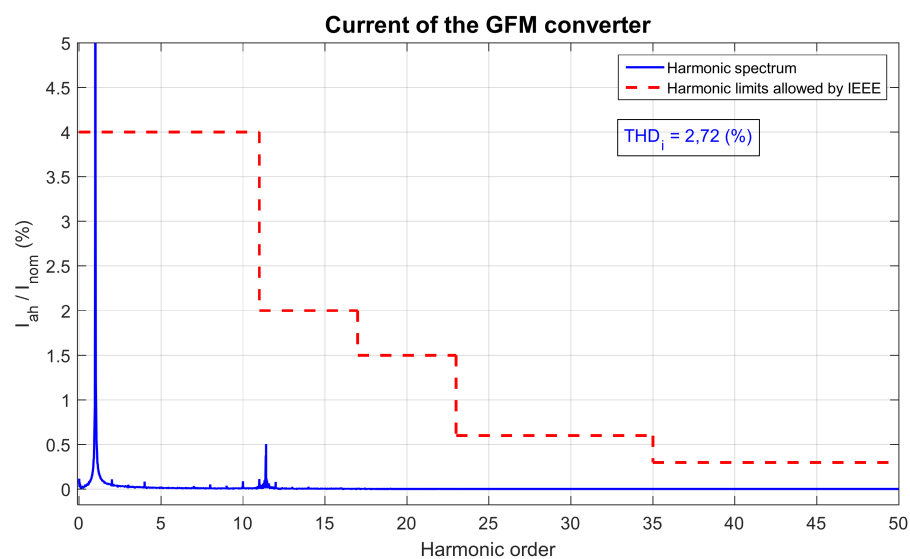


Figure 24. Frequency analysis of harmonic components.

To improve the presentation of the harmonic spectrum, the current amplitude in the fundamental harmonic is shown cropped in width. As the THD_i value (2.72 %) is less than 5 % and the harmonics do not exceed the allowed limits, the model is operated according to IEEE 1547 standard.

5. Conclusions

The main conclusion of this paper, based on the results obtained in the tests, is that the proposed mechanism can correctly provide the inertia emulation. Instability is avoided through the proposed PSS.

For the case in which no primary regulation is provided ($D = 0$), the inclusion of the PSS causes the displacement of the poles located on the imaginary axis, significantly improving system stability. This paper also explains the effect of the inertia constant value in GFM stability. Higher values of J decrease the speed of response of the system and increase the contribution of active power during frequency changes.

The findings of the paper were validated through a Hardware in the loop set-up in a real-time simulator. It was proved that the converter maintains the synchronism with the grid once it is synchronized and the main switch is closed. Furthermore, it was verified that the system provides active power following the changes in grid frequency, improving both the RoCoF and the nadir of the frequency change.

Finally, the converter's ability to switch from grid-connected mode to islanded mode was also validated. The GFM converter is able to maintain a constant voltage and frequency, demonstrating its ability to work as a voltage source emulating the behavior of a synchronous generator, supplying active and reactive power demanded by the system load.

Author Contributions: Conceptualization, J.L.R.A. and S.A.; Methodology, J.L.R.A.; Software, J.D.; Validation, J.D., J.L.R.A. and J.E.-G.; Investigation, J.L.R.A. and S.A.; Data curation, J.L.R.A. and S.A.; Writing—original draft preparation, J.D. and J.L.R.A.; Writing—review and editing, J.E.-G. and S.A.; Visualization, J.D.; supervision, J.L.R.A., S.A. and J.E.-G. All authors have read and agreed to the published version of the manuscript.

Funding: This paper was supported by the Spanish Research Agency under project reference PID2019-106028RB-I00/AEI/10.13039/501100011033.

Conflicts of Interest: The authors declare no conflict of interest.

Appendix A

RSCAD Parameters

Table A1 shows all the parameters used to configure the system in RSCAD.

Table A1. System parameters.

Parameters	Value	Units
DC voltage of the VSC, V_{dc}	1200	V
Converter rated power, S_n	2	MVA
Line to line rated voltage (RMS), V_n	690	V
Filter inductance, L_f	0.113	mH
Filter resistance, R_f	3.552	m Ω
Filter capacitance, C_f	1	mF
Nominal frequency, f_n	50	Hz
Switching frequency, f_{sw}	3	kHz
Synchronization constant, K_s	6.67	Hz/MVA
Grid inductance, L_g	0.226	μ H
Grid resistance, R_g	7.104	$\mu\Omega$
Short-circuit ratio, SCR	500	
X/R ratio	10	
Synchronous generator rated power, S_n	4.5	MVA
Synchronous generator Phase rated voltage, V_s	5	kV
Frequency, f_{sg}	50	Hz
Inertia constant, H_{sg}	2.5	s
Stator leakage reactance, X_a	0.113	p.u.
Unsaturated reactance, X_d	1.85	p.u.
Unsaturated transient reactance, $X_{d'}$	0.225	p.u.
Unsaturated sub-transient reactance, $X_{d''}$	0.2	p.u.
Q-axis unsaturated reactance, X_q	1.74	p.u.
Q-axis unsaturated transient reactance, $X_{q'}$	0.306	p.u.
Q-axis unsaturated sub-transient reactance, $X_{q''}$	0.2	p.u.
T_t : power rating, S_N	2	MVA
T_t : rated line-line voltage primary, V_{1N}	20	kV
T_t : rated line-line voltage secondary, V_{2N}	0.69	kV
T_t : frequency	50	Hz
T_g : power rating, S_N	4.5	MVA
T_g : rated line-line voltage primary, V_{1N}	5	kV
T_g : rated line-line voltage secondary, V_{2N}	20	kV
T_g : frequency	50	Hz

Appendix B

Active Power Synchronization Loop Parameters

The values used in the active power synchronization loop are shown in Table A2.

Table A2. Control loop parameters.

Parameters	Value	Units
Inertia constant, H	30	s
Damping constant, D	0	p.u.
PSS time constant, T_w	1.2	s
PSS constant, K_w	0.01	s

Appendix C

IEEE Maximum Harmonic Current Distortion in Percent of Rated Current

Table A3. IEEE 1547 Maximum odd harmonic current distortion in percent of rated current.

Individual Odd Harmonic Order, h	Percent (%)
$h < 11$	4.0
$11 \leq h < 17$	2.0
$17 \leq h < 23$	1.5
$23 \leq h < 35$	0.6
$35 \leq h < 50$	0.3
Total rated current distortion (RTD)	5.0

Table A4. IEEE 1547 Maximum even harmonic current distortion in percent of rated current.

Individual Odd Harmonic Order, h	Percent (%)
$h = 2$	4.0
$h = 4$	2.0
$h = 6$	1.5
$8 \leq h < 50$	Associated range specified in Table A1

References

- Matevosyan, J.; MacDowell, J.; Badrzadeh, B.; Cheng, C.; Dutta, S.; Rao, S.D.; Gevorgian, V.; Green, T.; Howard, D.; Kong, D.; et al. Grid-Forming Technology in Energy Systems Integration. ESIG High Share of Inverter-Based Generation Task Force: Report. Available online: <https://www.esig.energy/wp-content/uploads/2022/03/ESIG-GFM-report-2022.pdf> (accessed on 20 June 2022).
- Christensen, P.; Andersen, G.K.; Seidel, M.; Bolik, S.; Engelken, S.; Kneuppel, T.; Krontiris, A.; Wuerflinger, K.; Bülo, T.; Jahn, J. High Penetration of Power Electronic Interfaced Power Sources and the Potential Contribution of Grid Forming Converters. ENTSO-E: Report. Available online: <https://euagenda.eu/upload/publications/untitled-292051-ea.pdf> (accessed on 20 June 2022).
- Bialek, J.; Bowen, T.; Green, T.; Lew, D.; Li, Y.; MacDowell, J.; Matevosyan, J.; Miller, N.; O'Malley, M.; Ramasubramanian, D. System Needs and Services for Systems with High IBR Penetration. Global Power System Transformation Consortium (G-PST): Report. Available online: <https://globalpst.org/wp-content/uploads/GPST-IBR-Research-Team-System-Services-and-Needs-for-High-IBR-Networks.pdf> (accessed on 20 June 2022).
- Rosso, R.; Wang, X.; Liserre, M.; Lu, X.; Engelken, S. Grid-forming converters: Control approaches, grid-synchronization, and future trends-A review. *IEEE Open J. Ind. Appl.* **2021**, *2*, 93–109. [CrossRef]
- Rathnayake, D.B.; Akrami, M.; Phurailatpam, C.; Me, S.P.; Hadavi, S.; Jayasinghe, G.; Zabihi, S.; Bahrani, B. Grid Forming Inverter Modeling, Control, and Applications. *IEEE Access* **2021**, *9*, 114781–114807. [CrossRef]
- Zhang, H.; Xiang, W.; Lin, W.; Wen, J. Grid forming converters in renewable energy sources dominated power grid: Control strategy, stability, application, and challenges. *J. Mod. Power Syst. Clean Energy* **2021**, *9*, 1239–1256. [CrossRef]
- Chandorkar, M.C.; Divan, D.M.; Adapa, R. Control of parallel connected inverters in standalone AC supply systems. *IEEE Trans. Ind. Appl.* **1993**, *29*, 136–143. [CrossRef]
- Guerrero, J.M.; Vicuna, L.G.; Matas, J.; Castilla, M.; Miret, J. A wireless controller to enhance dynamic performance of parallel inverters indistributed generation systems. *IEEE Trans. Power Electron.* **2004**, *19*, 1205–1213. [CrossRef]
- De Brabandere, K.; Bolsens, B.; van den Keybus, J.; Woyte, A.; Driesen, J.; Belmans, R. A voltage and frequency droop control method for parallel inverters. *IEEE Trans. Power Electron.* **2007**, *22*, 1107–1115. [CrossRef]
- Guerrero, J.M.; de Vicuna, L.G.; Matas, J.; Castilla, M.; Miret, J. Output impedance design of parallel-connected UPS inverters with wireless load-sharing control. *IEEE Trans. Ind. Electron.* **2005**, *52*, 1126–1135. [CrossRef]
- Huang, L.; Xin, H.; Dörfler, F. H_∞ -control of grid-connected converters: Design, objectives and decentralized stability certificates. *IEEE Trans. Smart Grid* **2020**, *11*, 3805–3816. [CrossRef]
- Sharma, R.K.; Mishra, S.; Pullaguram, D. A robust H_∞ multivariable stabilizer design for droop based autonomous AC microgrid. *IEEE Trans. Power Syst.* **2020**, *35*, 4369–4382. [CrossRef]
- Pogaku, N.; Prodanovic, M.; Green, T.C. Modelling, analysis and testing of autonomous operation of an inverter-based microgrid. *IEEE Trans. Power Electron.* **2007**, *22*, 613–625. [CrossRef]
- Hart, P.; Lesieutre, B. Energy function for a grid-tied, droop-controlled inverter. In Proceedings of the 2014 North American Power Symposium (NAPS), Pullman, DC, USA, 24 November 2014.
- D'Arco, S.; Suul, J.A. Equivalence of Virtual Synchronous Machines and Frequency-Droops for Converter-Based MicroGrids. *IEEE Trans. Smart Grid* **2014**, *5*, 394–395. [CrossRef]

16. Zhang, L.; Harnefors, L.; Nee, H.-P. Power-synchronization control of grid-connected voltage-source converters. *IEEE Trans. Power Syst.* **2010**, *25*, 809–820. [[CrossRef](#)]
17. Harnefors, L.; Hinkkanen, M.; Riaz, U.; Rahman, F.M.M.; Zhang, L. Robust analytic design of power-synchronization control. *IEEE Trans. Ind. Electron.* **2019**, *66*, 5810–5819. [[CrossRef](#)]
18. Beck, H.-P.; Hesse, R. Virtual synchronous machine. In Proceedings of the 9th International Conference on Electrical Power Quality and Utilisation, Barcelona, Spain, 9–11 October 2007; pp. 1–6.
19. Chen, Y.; Hesse, R.; Turschner, D.; Beck, H. Comparison of methods for implementing virtual synchronous machine on inverters. In Proceedings of the International Conference on Renewable Energies and Power Quality, Santiago de Compostela, Spain, 28–30 March 2012.
20. Driesen, J.; Visscher, K. Virtual synchronous generators. In Proceedings of the IEEE Power and Energy Society General Meeting—Conversion and Delivery of Electrical Energy in the 21st Century, Pittsburgh, PA, USA, 20–24 July 2008.
21. Guan, M.; Pan, W.; Zhang, J.; Hao, Q.; Cheng, J.; Zheng, X. Synchronous generator emulation control strategy for voltage source converter (VSC) stations. *IEEE Trans. Power Syst.* **2015**, *30*, 3093–3101. [[CrossRef](#)]
22. Liu, J.; Miura, Y.; Ise, T. Comparison of dynamic characteristics between virtual synchronous generator and droop control in inverter-based distributed generators. *IEEE Trans. Power Electron.* **2016**, *31*, 3600–3611. [[CrossRef](#)]
23. Alipoor, J.; Miura, Y.; Ise, T. Power system stabilization using virtual synchronous generator with alternating moment of inertia. *IEEE J. Emerg. Sel. Top. Power Electron.* **2015**, *3*, 451–458. [[CrossRef](#)]
24. Torres, M.A.L.; Lopes, L.A.C.; Morán, L.A.T.; Espinoza, J.R.C. Self-tuning virtual synchronous machine: A control strategy for energy storage systems to support dynamic frequency control. *IEEE Trans. Energy Convers.* **2014**, *29*, 833–840. [[CrossRef](#)]
25. Li, D.; Zhu, Q.; Lin, S.; Bian, X.Y. A self-adaptive inertia and damping combination control of VSG to support frequency stability. *IEEE Trans. Energy Convers.* **2017**, *32*, 397–398. [[CrossRef](#)]
26. Wang, F.; Zhang, L.; Feng, X.; Guo, H. An adaptive control strategy for virtual synchronous generator. *IEEE Trans. Ind. Appl.* **2018**, *54*, 5124–5133. [[CrossRef](#)]
27. Van Wesenbeeck, M.P.N.; de Haan, S.W.H.; Varela, P.; Visscher, K. Grid tied converter with virtual kinetic storage. In Proceedings of the IEEE Bucharest PowerTech, Bucharest, Romania, 28 June–2 July 2009.
28. Mo, O.; D’Arco, S.; Suul, J.A. Evaluation of Virtual Synchronous Machines with Dynamic or Quasi-Stationary Machine Models. *IEEE Trans. Ind. Electron.* **2017**, *64*, 5952–5962. [[CrossRef](#)]
29. Rodríguez, P.; Candela, J.I.; Rocabert, J.; Teodorescu, R. Synchronous Power Controller for a Generating System Based on Static Power Converters. International Patent WO 2012/117 131 A1, 7 September 2012.
30. D’Arco, S.; Suul, J.A.; Fosso, O.B. Control system tuning and stability analysis of Virtual Synchronous Machines. In Proceedings of the 2013 IEEE Energy Conversion Congress and Exposition, ECCE 2013, Denver, CO, USA, 15–19 September 2013.
31. Liu, J.; Miura, Y.; Bevrani, H.; Ise, T. Enhanced virtual synchronous generator control for parallel inverters in microgrids. *IEEE Trans. Smart Grid* **2017**, *8*, 2268–2277. [[CrossRef](#)]
32. Zhang, W.; Cantarellas, A.M.; Rocabert, J.; Luna, A.; Rodríguez, P. Synchronous power controller with flexible droop characteristics for renewable power generation systems. *IEEE Trans. Sustain. Energy* **2016**, *7*, 1572–1582. [[CrossRef](#)]
33. Zhang, W.; Tarraso, A.; Rocabert, J.; Luna, A.; Candela, J.I.; Rodríguez, P. Frequency support properties of the synchronous power control for grid-connected converters. *IEEE Trans. Ind. Appl.* **2019**, *55*, 5178–5189. [[CrossRef](#)]
34. Quan, X.; Huang, A.Q.; Yu, H. A novel order reduced synchronous power control for grid-forming inverters. *IEEE Trans. Ind. Electron.* **2020**, *67*, 10989–10995. [[CrossRef](#)]
35. Meng, X.; Liu, J.; Liu, Z. A generalized droop control for grid-supporting inverter based on comparison between traditional droop control and virtual synchronous generator control. *IEEE Trans. Power Electron.* **2019**, *34*, 5416–5438. [[CrossRef](#)]
36. Baltas, G.N.; Lai, N.B.; Marin, L.; Tarrasó, A.; Rodríguez, P. Grid-forming power converters tuned through artificial intelligence to damp subsynchronous interactions in electrical grids. *IEEE Access* **2020**, *8*, 93369–93379. [[CrossRef](#)]
37. Qoria, T.; Rokrok, E.; Bruyere, A.; François, B.; Guillaud, X. A PLL-free grid-forming control with decoupled functionalities for high-power transmission system applications. *IEEE Access* **2020**, *8*, 197363–197378. [[CrossRef](#)]
38. Karimi, A.; Khayat, Y.; Naderi, M.; Dragicevic, T.; Mirzaei, R.; Blaabjerg, F.; Bevrani, H. Inertia response improvement in AC microgrids: A fuzzy-based virtual synchronous generator control. *IEEE Trans. Power Electron.* **2020**, *35*, 4321–4331. [[CrossRef](#)]
39. Zhong, Q.-C.; Weiss, G. Synchronverters: Inverters that mimic synchronous generators. *IEEE Trans. Ind. Electron.* **2011**, *58*, 1259–1267. [[CrossRef](#)]
40. Zhong, Q.-C.; Nguyen, P.-L.; Ma, Z.; Sheng, W. Self-synchronized synchronverters: Inverters without a dedicated synchronization unit. *IEEE Trans. Power Electron.* **2014**, *29*, 617–630. [[CrossRef](#)]
41. Wang, X.; Chen, L.; Sun, D.; Zhang, L.; Nian, H. A modified self-synchronized synchronverter in unbalanced power grids with balanced currents and restrained power ripples. *Energies* **2019**, *12*, 923. [[CrossRef](#)]
42. Dong, S.; Chen, Y.C. Adjusting synchronverter dynamic response speed via damping correction loop. *IEEE Trans. Energy Convers.* **2017**, *32*, 608–619. [[CrossRef](#)]
43. Dong, S.; Chen, Y.C. A method to directly compute synchronverter parameters for desired dynamic response. *IEEE Trans. Energy Convers.* **2018**, *33*, 814–825. [[CrossRef](#)]
44. Roldán-Pérez, J.; Rodríguez-Cabero, A.; Prodanovic, M. Design and analysis of virtual synchronous machines in inductive and resistive weak grids. *IEEE Trans. Energy Convers.* **2019**, *34*, 1818–1828. [[CrossRef](#)]

45. Jouini, T.; Arghir, C.; Dörfler, F. Grid-friendly matching of synchronous machines by tapping into the DC storage. *IFAC-PapersOnLine* **2018**, *49*, 192–197. [[CrossRef](#)]
46. Arghir, C.; Dörfler, F. The electronic realization of synchronous machines: Model matching, angle tracking, and energy shaping techniques. *IEEE Trans. Power Electron.* **2020**, *35*, 4398–4410. [[CrossRef](#)]
47. Johnson, B.B.; Dhople, S.V.; Hamadeh, A.O.; Krein, P.T. Synchronization of parallel single-phase inverters with virtual oscillator control. *IEEE Trans. Power Electron.* **2014**, *29*, 6124–6138. [[CrossRef](#)]
48. Johnson, B.B.; Dhople, S.V.; Cale, J.L.; Hamadeh, A.O.; Krein, P.T. Oscillator-based inverter control for islanded three-phase microgrids. *IEEE J. Photovolt.* **2014**, *4*, 387–395. [[CrossRef](#)]
49. Johnson, B.B.; Sinha, M.; Ainsworth, N.G.; Dörfler, F.; Dhople, S.V. Synthesizing virtual oscillators to control islanded inverters. *IEEE Trans. Power Electron.* **2016**, *31*, 6002–6015. [[CrossRef](#)]
50. Sinha, M.; Dörfler, F.; Johnson, B.B.; Dhople, S.V. Uncovering droop control laws embedded within the nonlinear dynamics of van der pol oscillators. *IEEE Trans. Control Netw. Syst.* **2017**, *4*, 347–358. [[CrossRef](#)]
51. Colombino, M.; Groÿ, D.; Dörfler, F. Global phase and voltage synchronization for power inverters: A decentralized consensus-inspired approach. In Proceedings of the 56th IEEE Conference on Decision and Control (CDC), Melbourne, Australia, 12–15 December 2017; pp. 5690–5695.
52. Colombino, M.; Groÿ, D.; Brouillon, J.; Dörfler, F. Global phase and magnitude synchronization of coupled oscillators with application to the control of grid-forming power inverters. *IEEE Trans. Autom. Control* **2019**, *64*, 4496–4511. [[CrossRef](#)]
53. Groÿ, D.; Colombino, M.; Brouillon, J.; Dörfler, F. The effect of transmission-line dynamics on grid-forming dispatchable virtualoscillator control. *IEEE Trans. Control Netw. Syst.* **2019**, *6*, 1148–1160.
54. Awal, M.A.; Yu, H.; Tu, H.; Lukic, S.M.; Husain, I. Hierarchical control for virtual oscillator based grid-connected and islanded microgrids. *IEEE Trans. Power Electron.* **2020**, *35*, 988–1001. [[CrossRef](#)]
55. Awal, M.A.; Yu, H.; Husain, I.; Yu, W.; Lukic, S.M. Selective harmonic current rejection for virtual oscillator controlled grid-forming voltage source converters. *IEEE Trans. Power Electron.* **2020**, *35*, 8805–8818. [[CrossRef](#)]
56. Awal, M.A.; Husain, I. United virtual oscillator control for grid-forming and grid-following converters. *IEEE J. Emerg. Sel. Top. Power Electron.* **2021**, *9*, 4573–4586. [[CrossRef](#)]
57. Bottrell, N.; Green, T.C. Comparison of current-limiting strategies during fault ride-through of inverters to prevent latch-up and wind-up. *IEEE Trans. Power Electron.* **2013**, *29*, 3786–3797. [[CrossRef](#)]
58. Golsorkhi, M.S.; Lu, D.D.C. A decentralized control method for islanded microgrids under unbalanced conditions. *IEEE Trans. Power Deliv.* **2015**, *31*, 1112–1121. [[CrossRef](#)]
59. Zarei, S.F.; Mokhtari, H.; Ghasemi, M.A.; Blaabjerg, F. Reinforcing fault ride through capability of grid forming voltage source converters using an enhanced voltage control scheme. *IEEE Trans. Power Deliv.* **2018**, *34*, 1827–1842. [[CrossRef](#)]
60. Lin, X.; Liang, Z.; Zheng, Y.; Lin, Y.; Kang, Y. A current limiting strategy with parallel virtual impedance for three-phase three-leg inverter under asymmetrical short-circuit fault to improve the controllable capability of fault currents. *IEEE Trans. Power Electron.* **2018**, *34*, 8138–8149. [[CrossRef](#)]
61. Hadavi, S.; Me, S.; Bahrani, B.; Fard, M.; Zadeh, A. Virtual Synchronous Generator Versus Synchronous Condensers: An Electromagnetic Transient Simulation-based Comparison. *Cigre Sci. Eng.* **2022**, *24*, 1–20.